J. Plasma Fusion Res. Vol.83, No.3 (2007) 215-227

Commentary

Ultra-Sensitive Measurement of Sheath Electric Fields by Laser-Induced Fluorescence-Dip Spectroscopy

CZARNETZKI Uwe and SASAKI Koichi[1]

Institute for Plasma and Atomic Physics, Ruhr-University Bochum, 44780 Bochum, Germany

[1]Department of Electrical Engineering and Computer Science, Nagoya University, Nagoya 464-8603, Japan

(Received 26 January 2007)

Laser spectroscopic electric field measurements have become a versatile tool for the diagnostics of low-temperature plasmas. High spatial and temporal resolutions can be achieved, and from the measured field structures, other important quantities like voltage, displacement current, or even the plasma density can be inferred directly. A variety of different techniques has been developed over the past two decades since the first experiments were performed by Gottscho in 1987. One of the most successful and sensitive techniques is fluorescence-dip spectroscopy. This general technique has been applied to hydrogen, helium, argon, krypton, and xenon discharges and gas mixtures containing theses gases. In this paper, an introduction to the technique with special emphasis to results obtained in hydrogen and argon is presented. Further a brief review on the general field of laser electric field measurement in low-temperature plasmas and related questions on use of the Stark effect is provided.

Keywords:

electric field, Stark spectroscopy, laser-induced fluorescence-dip spectroscopy, hydrogen, krypton, argon

1. Introduction

Electric fields play a fundamental role in plasmas. Particle transport, power coupling, and wave propagation are all related to electric field structures and dynamics. At the edge of plasmas, ions and secondary electrons can be accelerated to high energies in the sheaths. Moreover, in high frequency RF sheaths the dynamics of electron and electric fields are strongly coupled. Finally, even if there is no electric field on a macroscopic scale, quasi neutral plasmas can develop rather strong fields by the random ion charge distribution on scale lengths shorter than the Debye length. These microfields can lead to a substantial broadening of optical transitions and lowering of the ionization energy in atoms and molecules and are a measure of the plasma density.

A variety of different techniques have been developed for the measurement of electric fields in plasmas. Ambipolar fields can be measured rather conveniently with Langmuir or emissive probes [1, 2]. Induction or B-dot probes can be used for the detection of induced RF electric fields [3]. Optical emission spectroscopy allows the determination of microfields, especially at high plasma densities as they are found in *e.g.* pinches or arcs [4]. In recent years, substantial effort has been made on the development of sensitive laser techniques for electric field measurement in plasmas. This development has been motivated mostly by the investigation of the electric field structure in static and RF sheaths. Electric fields in sheaths are very important for the understanding of power coupling to the plasma, the transport of electrons and ions, and the ion-surface interaction. Laser techniques are non-intrusive and have the additional advantage of high spatial and temporal resolution which is ideal for sheaths with typical spatial extensions in the mm range and dynamics on an ns timescale.

We will first give an overview on the basic principles of laser Stark spectroscopy in plasmas and the commonly applied laser techniques (section 2). Within the limited frame of this review, the overview can only be a rough sketch and the intention is more on introducing the general ideas, problems, and techniques than to go very much into detail. For work before 1994, the reader might refer to the excellent review paper by Lawler and Doughty [5]. Another critical review by Muraoka *et al.* might also be referred [6]. The main focus of this review is on the application of fluorescence-dip spectroscopy to laser electric field measurement. In recent years this technique has applied successfully in a number of atomic systems and has allowed investigations on plasma and sheath phenomena that were not possible otherwise (section 3). Examples for the application in atomic hydrogen (section 4) and argon (section 5) will be given in the following chapters. The review closes with a summary and outlook (section 6).

authors' e-mail: Uwe.Czarnetzki@ep5.ruhr-uni-bochum.de, sasaki@nuee.nagoya-u.ac.jp

2. Electric Field Measurement by Stark Spectroscopy

Neutral atoms or molecules are naturally present in low-temperature plasmas and often certain traces can be added without altering the discharge characteristic. These neutral particles can serve as probes for electric field measurements. In highly excited Rydberg states, the electrons are on large orbits and the electric field of the core is relatively weak. Therefore, already small external fields can change the eigenstates and eigenfunctions of the electron and states are shifted and mixed by the Stark effect. Generally, the Stark effect increases with the principle quantum number n approximately like n^2. The related optical line shifts or the amplitude of otherwise forbidden transitions can be measured with high sensitivity by laser spectroscopy. These investigations were started by R. Gottscho in 1987 on BCl in a BCl_3 discharge [7], and since then a large variety of different atomic (H, He, Ne, Ar, Kr, Xe) and bi-molecular systems (BH, CS, NaK) as well as laser spectroscopic techniques has been applied [5–39]. Depending on the particular scheme, the lowest detectable fields range from a few V/cm to several 100 V/cm. All these techniques are limited to low pressures where quenching is weak. A so far unique exception is the technique developed by Ochkin and co-workers in 1995 which is based on a CARS (Coherent Anti-Stokes Raman Scattering) like four-wave mixing technique and allows in principle single shot electric field measurement [37, 38]. It requires molecular probes like H_2 and works at atmospheric pressures or above. However, in this review, we will concentrate on low-pressure applications of typically less than a few 100 Pa where quenching is weak or can be neglected [40].

The Stark effect usually couples different angular momentum states of the same principal quantum number n. These states are energetically close and mixing can be strong. States at different principal quantum number, that are further away, contribute substantially less. However, this clear order is present only in atomic hydrogen and certain deviations can occur in many electron atoms like *e.g.* krypton. Since n is larger, also the number of angular momentum states is large and the spectrum can become quite complex. In order to understand the basic physics, one can concentrate on a simple model system consisting of only two states with wavefunctions $\Psi_{1/2}$ which are located symmetrically at energies $E_{1/2} = \pm\Delta$. Due to selection rules, only one of these states might be connected to a lower state by an optical dipole transition. Here the Ψ_1 state is chosen. If an electric field F is applied, new eigenfunctions $\varphi_\pm$ with new energies $E_\pm$ result that are a superposition of the undisturbed eigenfunctions. In this simple case, it is easy to calculate exactly the solution from Schrödinger's equation:

$$\varphi_\pm = a_\pm \Phi_1 + b_\pm \Phi_2 \tag{1}$$

and

$$E_\pm = \pm\sqrt{1 + |W|^2} \tag{2}$$

with

$$W = \left\langle \Psi_1 \middle| \vec{d} \cdot \vec{F} \middle| \Psi_2 \right\rangle / \Delta \tag{3}$$

and

$$a_\pm = \left[1 + \left|\frac{W}{E_\pm}\right|^2\right]^{-1}, \qquad |b_\pm|^2 = 1 - |a_\pm|^2, \tag{4}$$

where W is the matrix element normalized to Δ and $\vec{d} = -e\vec{r}$ is the dipole operator. W can be viewed as a normalized field strength. The results depend only on the absolute value of W, i.e. they are independent of sign of the electric field that has to be inferred otherwise. A plot is shown in **Fig. 1**. At vanishing field strength, the undisturbed energies result (**Fig. 1(b)**), but at finite but small values $0 < W < 1$, the energies are shifted approximately quadratically with W, and for $W \gg 1$, the shift is linear. This means that the Stark effect is quadratic as long as the additional energy of the electron in the external field is smaller than the separation between the states involved. In hydrogen, all states are effectively degenerate ($\Delta = 0$) and a linear Stark effect is observed at all field strengths. In multi-electron atoms, the fine-structure shift is much stronger and only states with high angular momentum are degenerate, i.e. Δ can be quite large. The quadratic Stark effect leads to very small shifts at low field strengths and, therefore, has a lower sensitivity than the linear Stark effect.

The state mixing becomes obvious in **Fig. 1(a)**. At zero

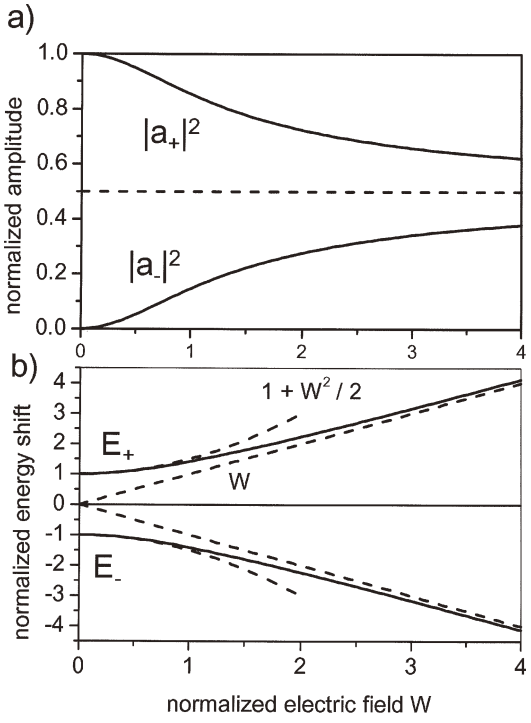

Fig. 1 Stark effect in a two-level system: a) amplitudes for dipole-transition to lower state, b) shift of the new eigenstates. The broken lines indicate the approximate behavior at low (quadratic) and high (linear) field strengths.

field, the new eigenfunctions are identical to the initial eigenfunctions. With increasing field strength, the upper state φ_+ receives a growing admixture of the Ψ_2 state while the contribution of the initial Ψ_1 state decreases. The lower state develops just oppositely. Since it has been assumed initially that only the Ψ_1 state has an allowed optical transition, the observed intensity is directly proportional to the coefficients $|a_\pm|^2$. This means that the initially allowed transition to the upper state becomes weaker with increasing field strength and the initially forbidden transition to the lower state grows in strength. In this example, both states show equal intensity at infinite field strength. At very low field strength, the quadratic Stark shift might be difficult to observe. However, the intensity ratio of the initially allowed and forbidden transition is often much easier observed. Especially at low field strength, this ratio varies strongly with the field strength. In fact, this is the way the Stark effect is measured in diatomic molecules. The higher angular momentum states (f, g, …) in Rydberg levels of multi-electron atomic systems are often approximately degenerate and show a linear Stark effect. However, due to selection rules, transitions to these states are forbidden from commonly accessible lower states like *ns* or *np*. Only at higher field strengths, the increasing admixture of the *s* and *p* states makes an observation of the linear Stark effect possible.

In more realistic atomic systems, the calculation works very similar [41, 42]. However, the increasing number of states does no longer allow for an analytical solution and the related sets of linear algebraic equations have to be solved numerically. This can be performed relatively easily for atomic hydrogen. In multi-electron atoms, an increasing complexity in the coupling of the different angular moments arises and often reliable matrix elements are not available. Especially for low angular momentum states, the wavefunctions show a non-vanishing amplitude at the core and are strongly influenced by the nucleus and the core electrons which makes calculations quite difficult. Nevertheless, there has been substantial progress in recent years in the calculation of the Stark effect in noble gases and also in molecules [10, 12, 16, 24, 26, 28, 32, 34].

Additional to calculations, calibration measurements are usually performed. Here the probe atoms are placed in a homogeneous electric field which is typically generated between two planar electrodes. In order to avoid electrical breakthrough and collisional quenching, the pressure is normally chosen well on the left side of the Paschen curve. For schemes which require population in metastable states, these states have to be prepared in an external discharge like in a flow-tube system. Care has to be taken to keep the calibration region free from residual charges generated in the external discharge. This can be achieved by placing mesh electrodes or perpendicular magnetic fields in the gas flow between the discharge and the calibration region.

Laser spectroscopic techniques for the measurement of the Stark effect in plasmas can be divided into two categories: optogalvanic detection and fluorescence detection. In optogalvanic detection, the ionization probability of an atom is changed by laser excitation to a Rydberg state. This leads then to a change of the discharge current by charge multiplication, that can be easily detected as a short AC signal if the laser is pulsed, typically on a ns timescale. The electric field is inferred by measuring the detailed spectrum of a particular transition by tuning the laser frequency over the resonance. These techniques are very sensitive and ideal for DC or low frequency discharges over small electrode areas. The laser beam is focused in order to achieve the required spatial resolution and the entire beam path in the sheath contributes which leads to a limit on the electrode size. The optogalvanic signal is usually on a much longer timescale than the laser pulse and does not allow the temporal resolution required for RF discharges. The spatial structure of the electric field in the sheath is obtained by successive measurements at different sheath positions.

The detection of fluorescence light emitted from the excited Rydberg state provides the opportunity of direct spatial resolution within the laser beam cross section by adequate imaging. Thereby the need of focusing is avoided. Further, and maybe even more important, it allows high temporal resolution since the limiting factor is now only the laser pulse width. The electric field and the related Stark effect on the atom are only probed during the short interaction time between the laser radiation and the atomic transition, although the subsequent fluorescence light might be emitted on a much longer timescale. Typically, Nd:YAG pumped dye or OPO (Optical Parametric Oscillator) systems with subsequent frequency doubling or tripling are used which have pulse widths of about 5 ns. This is short compared to the period of 74 ns of typical RF discharges at 13.56 MHz. In principle, even shorter pulse widths could be used. The laser systems mentioned above all operate on a number of spectral modes with a total spectral width of typically about 0.1 cm^{-1}. Therefore, with the same spectral resolution a single mode laser could have a pulse width of the order of 0.1 ns. However, such systems are not easily available.

The laser excitation of Rydberg states is a general problem for both techniques. By definition, Rydberg states have a high excitation energy and this usually does not allow direct excitation from the ground state by radiation in the visible or UV. For this reason, the use of most atomic probe systems is based on a sufficient population of metastable states by collisional processes in the plasma, i.e. mostly by electrons. From this elevated initial state, further excitation to the Rydberg state becomes feasible, as is the case for helium, neon, and argon. Alternatively, an intermediate state can also be populated temporarily from the ground state by a two-photon excitation using a second pulsed laser system. Both laser pulses need to be synchronized since the lifetime of the intermediate state is typically of the order of 10 ns. The advantage is that now the much higher population of the ground state can be accessed and the technique becomes independent from sufficient excitation by the plasma. The former point provides the opportunity to admix small amounts of the probe gas as a tracer to complex molecular gas mixtures, and the latter point

becomes important at low electron densities or high quenching of the metastable state by collisions. However, the available photon energy for the two-photon excitation is limited ($\lambda >$ 203 nm), and only hydrogen, krypton, and xenon have been used so far. It should be noted that also N, O, C, and Cl can be two-photon excited, although they have not been applied as atomic probes for electric field measurement yet.

A general problem of fluorescence light detection is that the long lifetime of Rydberg states leads to very small emission amplitudes. This is especially troublesome since the lifetime increases with the principal quantum number approximately like n^3 while the Stark effect increases only like n^2. This limits the maximum n and thereby the field sensitivity. Nevertheless, in atomic hydrogen, Stark splitting in sheaths has been measured by direct fluorescence spectroscopy with states ranging from $n = 2$ to $n = 6$. In order to overcome this general shortcoming, Greenberg and Hebner used successfully a collisional population transfer from the singlet to the triplet system in helium [11, 12]. The laser excitation is between a metastable 2*s* and an *np* Rydberg state (typically n =11) in the singlet system. At high n, the singlet states are energetically very close to the triplet states, and electron and neutral collisions can both lead to a population transfer. The advantages are that the lifetime of the triplet system is much shorter (but still of the order of several 100 ns) and that the emission wavelength is different from the laser wavelength.

In atomic hydrogen, an interesting alternative has been developed by de la Rosa *et al.* [39]. This polarization spectroscopic technique is effectively a kind of four-wave mixing. It requires rather high atomic hydrogen densities as can be found in arcs or hollow cathode discharge where the method has been applied. The technique is based on a two-photon transition between the 1*s* ground state and the 2*s* state, and the polarization of a probe beam is measured. The electric field strength is inferred from the spectral width of the absorption profile, and a lower limit for the resolved field of about 2 kV/cm was achieved. The advantage is that background emission from the plasma is strongly suppressed by detecting light only within the small solid angle of the probe beam. Polarization techniques have been applied also by Oda *et al.* in herium under the presence of a magnetic field [35, 36].

3. Principles of Laser-Induced Fluorescence-Dip Spectroscopy

One of the main problems related to fluorescence spectroscopy is the long lifetime of Rydberg states that setting limits to the maximum quantum states. In order to overcome this limit, fluorescence-dip spectroscopy was introduced for electric field measurements in 1997 [17]. The technique was first applied to atomic hydrogen, and has been adopted for xenon, krypton, and in modified versions also to helium and argon. It is similar to scheme applied earlier for the measurement of excited states in molecular Nitrogen [43]. A general scheme is shown in **Fig. 2**. The basic idea is to excite first with one laser beam from a lower state (1) a short living intermediate state (2) from where fluorescence light emitted by

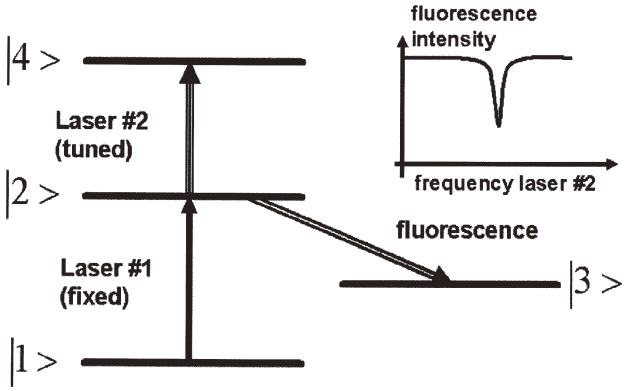

Fig. 2 General scheme for fluorescence-dip spectroscopy.

a transition to a lower state (3) can be observed conveniently. Then a second laser beam is tuned in resonance between this intermediate state (2) and a highly excited Rydberg state (4). If both lasers are pulsed, the second excitation can efficiently transfer a substantial part of the population of the intermediate state to the Rydberg state. Consequently, fluorescence from the intermediate state will decrease. The Rydberg spectrum can now be measured by keeping the first laser frequency fixed on resonance between the lower and the intermediate state and tuning the second laser frequency. The various resonances are observed as dips in the fluorescence originating from the intermediate state. Therefore, the lifetime of the Rydberg state does not affect the observed signal. Nevertheless, with increasing lifetime also the transition moment decreases and the energy necessary for depletion of the population of the intermediate state increases. An order of magnitude formula for the necessary energy can be derived from a simple rate equation analysis of a two-level system. The energy necessary for sufficient depletion of the population of the intermediate state is then given by:

$$E_s = \frac{8\pi hc\Delta\nu S}{\lambda^3 A_{ir}} . \quad (5)$$

Here h is the Planck constant, c the speed of light, $\Delta\nu$ the spectral width of the laser radiation between the intermediate and the Rydberg state, λ the laser wavelength, S the beam cross section, and A_{ir} the Einstein coefficient for the transition. The result is independent of the laser pulse width since the amount of transferred population depends only on the product of intensity and interaction time. With ns pulses and energies up to some mJ, Rydberg states up to $n = 50$ can be observed readily.

Care might also be taken with respect to the population of the intermediate level 2. Amplified stimulated emission can occur along the axis of the beam of the first laser if the population exceeds a certain threshold N_{2C}. An order of magnitude formula can be derived taking into account amplification from quantum noise to a significant intensity:

$$N_{2C} = \frac{\omega^2 \Delta_D}{c^2 A_{23} L} , \quad (6)$$

where $\omega = 2\pi c/\lambda$. For the Balmer-α transition in atomic hydrogen, a Doppler width Δ_D at room temperature, and an amplification (focal) length of $L = 1$ cm, the critical density is about $N_{2C} = 1 \times 10^{13}$ cm^{-3}. Generally, such a high population leads also to strong fluorescence signals and the pumping laser intensity can easily be adjusted.

In atomic hydrogen, level 1 is the ground state $n = 1$, intermediate level 2 is $n = 3$, level 3 is $n = 2$, and level 4 is a Rydberg state with $n \gg 3$. The excitation from the ground state to the intermediate level is provided by two-photon excitation at $\lambda = 205$ nm. In order to achieve a better efficiency, two counter propagating UV beams allow Doppler-free two-photon excitation. Florescence light is observed at Balmer-α (656 nm). The near IR radiation for the excitation to the Rydberg level can be generated conveniently by Raman shifting laser radiation in the visible to the first Stokes component in a high pressure cell filled with molecular hydrogen at typically 30 bar to 40 bar. This has the advantage of operating the laser in the visible between about 600 nm and 660 nm instead of near IR, and it extends the wavelength tuning range by about a factor two from approximately 800 nm to 910 nm.

At the moderate level $n = 6$, both diagnostics, conventional fluorescence and fluorescence-dip spectroscopy, are possible and the spectra can be compared. The result is shown in **Fig. 3**, where the dip-spectrum has been inverted in order to give the spectrum a more convention appearance. Both spectra agree well but the dip-spectrum shows a better resolution.

The hydrogen ground state is 1*s* and the magnetic quantum number is $m = 0$. With linearly polarized radiation in the two-photon excitation only $m = 0$ states are populated in the intermediate $n = 3$ state. Then, with radiation from the second laser polarized parallel to the electric field, again only $m = 0$ states are populated in the Rydberg state. This allows a total number of Stark split states of $n + 1$, corresponding to the number of states with different angular momentum. For the above case of $n = 6$, this gives the observed number of seven. If n is even a central line appears and if n is odd the centre shows a void. With the second laser polarized perpendicular to the electric field, only $m = \pm 1$ states can be reached and the total number of lines is n. Then for even n the centre shows a void and for odd n a central line appears. This provides a convenient way for measuring the direction of the electric field by rotating the polarization of the second laser and detecting the relative strength of the central component. This is demonstrated in **Fig. 4** where the experimental result is compared to the expected scaling proportional to $\sin^2(\phi)$.

In atomic systems other than hydrogen the situation is more complex. There, the angular momentum states for a given principal quantum number n are no longer degenerate. Since the lower state is typically an *s*-state, the intermediate state is either a *s*- or *d*-state after two-photon excitation and a *p*-state in case of single photon excitation. This allows excitation in the Rydberg state to *f*-states or lower angular momentum states. The lower the angular momentum, the more pronounced is in general the deviation from degeneracy due to the fine structure. Further, the lower states receive a relative strong disturbance by the core electrons since the wavefunctions have a non-vanishing amplitude at the core. This leads to a quadratic Stark effect at low field strengths and a more complex polarization dependence. However, the higher angular momentum states are mostly degenerate, and so at very high electric fields when they are admixed to the lower angular momentum states at observable amplitudes, a linear Stark effect spectrum similar to hydrogen can be observed. An example in case of krypton is given in **Fig. 5** [34].

Highly excited states in the hydrogen atom all show a linear Stark effect which makes it ideal for electric field measurement. Even with the very low state $n = 3$, electric field measurements are possible. Using a single mode Fourier limited bandwidth laser system ($\Delta\nu = 0.004$ cm^{-1}) and Doppler-free two-photon excitation at 205 nm with counter propagating beams, Booth *et al.* achieved a sensitivity of about 100 V/cm [13]. However, this required a very specialized noncommercial laser system. With more standard systems, the

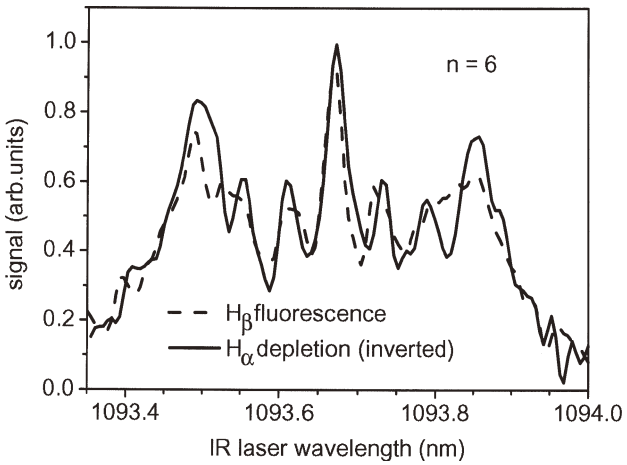

Fig. 3 Comparison between conventional fluorescence spectroscopy (detection at Balmer-δ) with fluorescence-dip spectroscopy (detection at Balmer-α) at $n = 6$. The electric field strength is 950 V/cm [17].

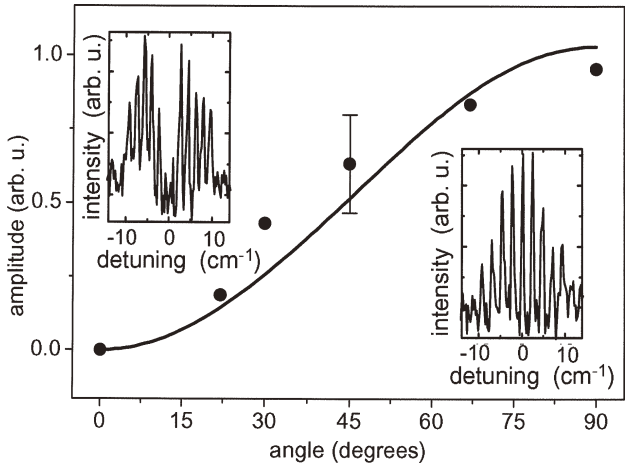

Fig. 4 Polarization dependence of the central line at $n = 14$ and an electric field of 950 V/cm. The solid line represents the theoretically expected dependence and the inserts show the spectra at $\phi = 0°$ and $\phi = 90°$ [17].

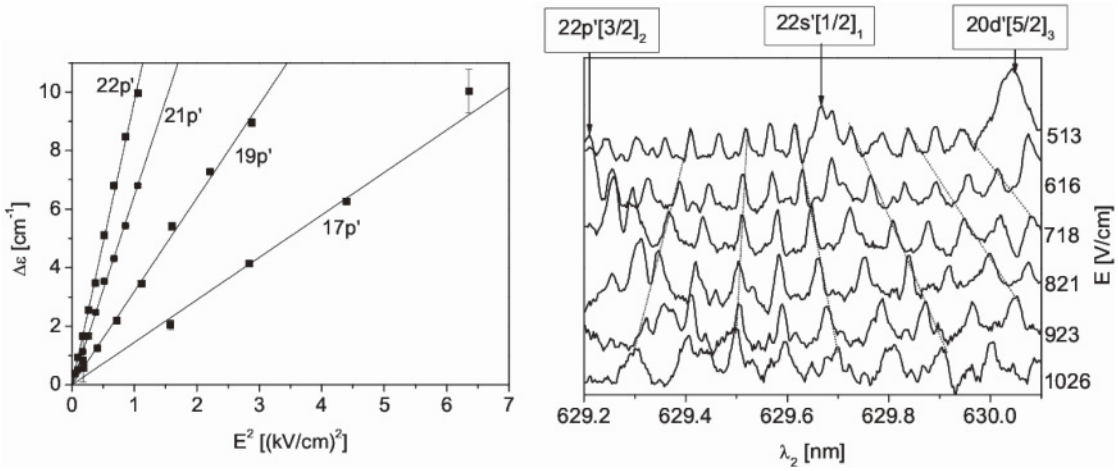

Fig. 5 Stark effect measured by fluorescence-dip spectroscopy in krypton: Quadratic Stark shift of the 17*p*′ to 22*p*′ levels (left figure). Linear Stark effect spectrum for the 19(*l*′ > 3) levels which spectrally overlap with the 22*s*′, 22*p*′, and 20*d*′ levels (right figure). The 19(*l*′ > 3) lines become visible only at fields above about 500 V/cm [34].

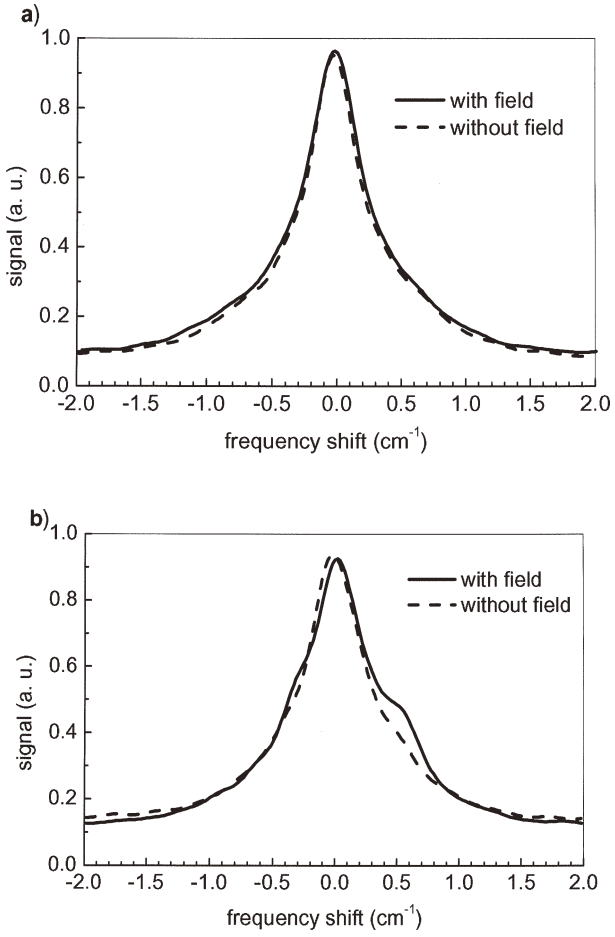

Fig. 6 Fluorescence signal at Balmer-α after two-photon excitation of atomic hydrogen at 205 nm to $n = 3$ as a function of the UV-laser frequency detuning from resonance. The measurement was taken in the sheath of a capacitively coupled RF discharge at 80 Pa. The electric field is about 1000 V/cm. a) laser electric field polarized perpendicular to the RF electric field, b) parallel polarization.

bandwidth is usually larger and a smaller sensitivity results as shown in **Fig. 6**. Here the Stark effect is strongly influenced by the fine structure splitting which is about the same order for fields at 1 kV/cm. This gives the spectrum a strong dependence on the polarization of the laser radiation relative to the electric field and the broadening is much more pronounced with parallel polarization as predicted by calculation [13]. The figure represents the lower limit of electric field measurement at about 1 kV/cm. A similar sensitivity was found by de La Rosa *et al.* by applying a kind of two-photon polarization spectroscopy technique [39].

Much higher sensitivities can be achieved by using Rydberg states with a principal quantum number $n \gg 3$. Here the fluorescence-dip technique allows probing of states up to about $n = 50$. The minimum detectable field is mostly limited by the finite bandwidth of the laser radiation and a slight broadening by the saturation introduced in order to observe easy detectable dip of typically a few 10% reduction of the fluorescence intensity. An upper limit is set by the overlap of Stark spectra from states with neighboring quantum numbers, i.e. $n - 1$ and $n + 1$. While the upper limit can be calculated, the lower limit depends on the experimental spectral resolution. One of the main limitations in resolution are fluctuations of the fluorescence intensity introduced by power, spatial beam profile, and especially spectral mode profile variations in the pump beam for the two-photon excitation. The related noise requires a certain dip strength for detection and this again is related to a certain saturation and line broadening. An experimental result is shown in **Fig. 7** where the spectral resolution is about $\Delta_0 = 0.57$ cm^{-1}. Typical error bars are indicated. The minimum electric field is then given for $n \gg 1$ by $E_{\min} \simeq \Delta_0/\alpha n^2$ and the maximum electric field by $E_{\max} \simeq 2R/\alpha n^5$ where $\alpha = 1.28 \times 10^{-4}$ V^{-1} is the Stark constant for atomic hydrogen and $R = 1.097 \times 10^5$ cm^{-1} the Rydberg constant. The theoretical curve for the minimum field fits very well to the experimental data and also the maximum field is confirmed for the higher quantum numbers where the corresponding field strength is realized in the experiment.

The spectrum in a transition between $n = 3$ and a Rydberg

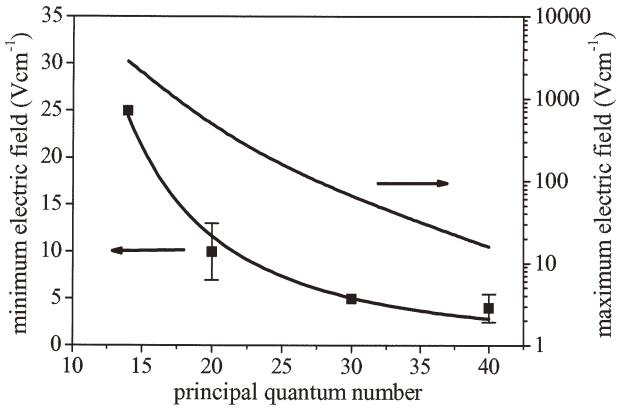

Fig. 7 Experimentally determined minimum detectable electric field strength and calculated maximum unambiguously detectable field strength in atomic hydrogen as a function of the principal quantum number *n*. The minimum electric field is also represented by the theoretical curve including the experimental spectral resolution.

state is determined predominantly by the Stark effect of the Rydberg state. However, as shown in **Fig. 6**, at high fields there is also a smaller Stark effect on $n = 3$. This additional effect can be minimized, if the UV laser is polarized perpendicular to the electric field. Nevertheless, even then it should be noted that at field strengths below 1 kV/cm, the Stark effect in $n = 3$ still leads to a mixture of the three angular momentum states. Without field and linear polarization of the two-photon exciting UV beam, mostly the 3*d* and to a smaller degree also the 3*s* state are populated while the 3*p* state remains unpopulated. Depending on the Stark mixing, the transition spectra to the Rydberg state then change their form slightly although the total width and the position of the individual lines remain unchanged.

Examples for the application of fluorescence dip spectroscopy to the investigation of hydrogen and argon containing discharges are presented in the following chapters.

4. Electric Field Measurements in Hydrogen Plasmas

Measurements of sheath electric field were performed in a capacitively coupled GEC (Gaseous Electronics Conference) reference cell at the standard RF frequency of $f = 13.56$ MHz [19–21]. The reactor is equipped by two coplanar electrodes with the upper electrode grounded and the RF power applied to the lower electrode. The electrode diameter is 10 cm and the separation 2.5 cm. The unfocussed laser beams are aligned parallel to the electrode surface, and the fluorescence light is imaged perpendicularly by a $f = 50$ mm lens onto a gated ICCD camera (Princeton Instruments). The spatial resolution in the vertical direction is 100 µm. The unfocussed laser beams allow fields to be measured in parallel within a width of up to about 3 mm. At each spectral position, fluorescence light is accumulated over several 100 laser shots and typically 100 spectral points are recorded for a full spectrum. The laser is locked to the RF phase and spatial field profiles are measured in small temporal steps of a few ns over the full period of the RF cycle.

An example for the two-dimensional electric field distribution above the powered electrode at maximum sheath extension is shown in **Fig. 8**. The effect of the grounded confinement ring at the right on the electric field distribution can be clearly recognized. The maximum field strength at the electrode surface is about 1.8 kV/cm and the sheath extension is about 6 mm.

The sheath electric field shows the same spatial-temporal structure over most of the radial extension. The axial field structure at various phases of the RF cycle is shown in **Fig. 9**, where also the related space charge density is displayed. The space charge density follows directly from the special derivative of the electric field by Poisson's equation. The parallel development of a field reversal where electrons are attracted to the electrode and a negative space charge region at the point of maximum sheath extension can be clearly identified. This field reversal is characteristic to hydrogen CCP (Capacitively-Coupled Plasma) discharges and is caused mostly by the low mass of the dominant ion species H_3^+ which provides

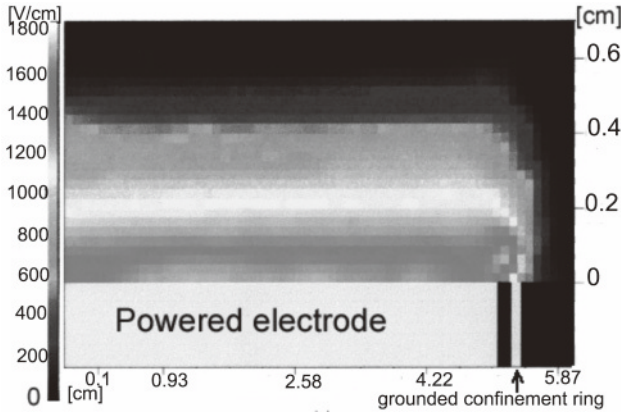

Fig. 8 Measured electric field distribution above the surface of a planar electrode in a CCP hydrogen discharge at 80 Pa and a negative potential of 500 V [19].

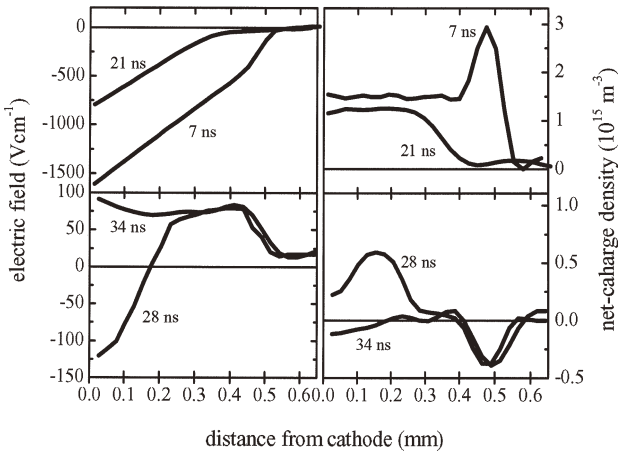

Fig. 9 Electric field structure and net-charge density in front of the powered electrode at various phases of the RF cycle [19].

an unusually high Bohm current and partly to the low mobility of electrons [19, 44].

Spatial integration of the electric field yields the sheath voltage. In **Fig. 10(a)**, the sheath voltages have been measured at the powered electrode and in front of the grounded electrode. The sum is compared to the applied voltage that has been measured by a high voltage probe. The small deviations of the probe voltage from a sinusoidal voltage form are caused by induction losses in the connection between the measurement point and the electrode.

The displacement current density follows from the temporal derivative of the electric field directly in front of the electrode (**Fig. 10(b)**). The displacement current at the electrode is continued in the quasi-neutral region of the discharge as a real flow of electrons. In comparison to this, the ion current has lower amplitude by about one order of magnitude. During the sheath collapse, electrons are flowing directly to the electrode, and this current is particularly pronounced due to the field reversal. During this period, the displacement current vanishes. The displacement current is approximately anti-symmetric with respect to the time of the sheath collapse and increases linearly from the minimum to the maximum value. During the sheath collapse, a rapid change of the sign occurs.

Microwave field oscillations are by far too fast to be resolved and many field oscillation periods occur within the interaction time of the atom with the laser field. However, due to the fact that the Stark effect depends only on the absolute value, the overall effect does not cancel out on average. Microwave discharges often operate at over critical densities and only an evanescent field can penetrate into the plasma over a short distance. Within this short distance, the density and electron temperature are very high, and both high microfield and high plasma background emission are unfavorable to the measurement of the microwave field. However, prior to plasma ignition during the switch-on phase, the density is still low and the microwave field can fill the entire discharge region. An example of time resolved microwave field measurement within this special temporal interval is shown in **Fig. 11** [22, 45].

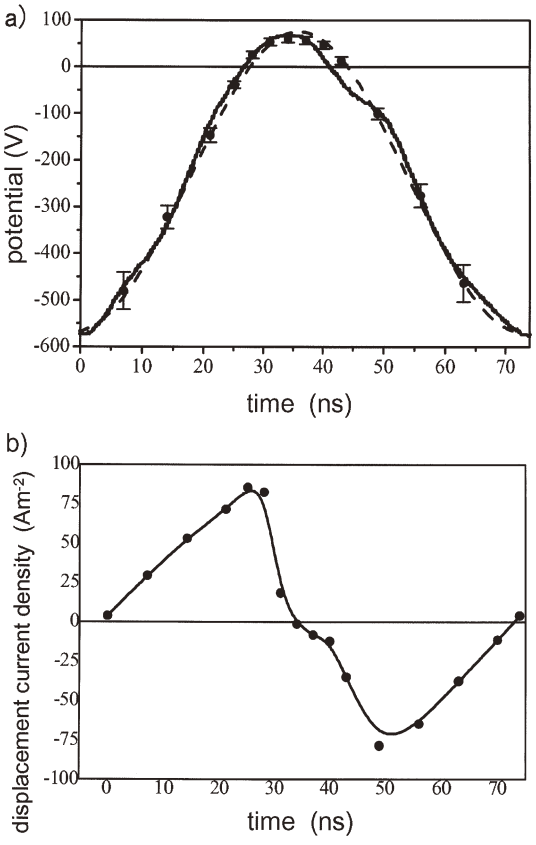

Fig. 10 a) Discharge voltage: from electric field measurements (points), sinusoidal fit (broken line), and high voltage probe measurement (solid line). b) Displacement current density (the solid line is a B-spline fit for better visibility) [19].

The measurement was performed in a commercial SLAN (Slot Antenna Microwave Plasma Source) reactor at 2.45 GHz where the microwave is distributed around a waveguide ring resonator [46]. At the inner side of this ring, the microwave is coupled to the plasma by 10 slit antennas. These antennas are separated by half a wavelength. The plasma is confined in a quartz cylinder of 16 cm diameter. The laser beam is sent through the antenna slits across the discharge and fluorescence light is observed by an ICCD camera from above. Data acquisition is similar to the case described above. Discharge conditions are: 40 Pa H_2, pulsed mode at f = 1.5 kHz with 50% on-time, average net power launched to the discharge P = 500 W, power of the magnetron source during the on-phase P = 1800 W.

The measurements show clearly that a standing wave structure is established that does not change much over time. However, the field amplitude of this standing field is increasing in time as the power coming from the magnetron source increases. As shown in **Fig. 11(b)**, a very good agreement is found between the temporal development of the relative field within the ring-resonator measured by a small antenna and the field in the discharge region. This confirms that the standing wave structure continues into the resonator as expected. At t = 4 μs, the ignition occurs and the field within the resonator breaks down temporally, while the plasma density rises strongly within a very short time interval. With increasing plasma density, absorption increases, the field can no longer penetrate into the discharge region which again increases the density and the electron temperature. However, this ignition phase is too irreproducible to allow laser electric field measurements which require acquisition over thousands of discharges.

At much later times stable discharge conditions are established. There the microwave penetrates only about 1 cm into the discharge region which is field free otherwise. Within a Debye radius the arbitrary distribution of ions leads to short scale microfields. Hydrogen atoms within the discharge are then exposed to a characteristic statistic distribution of field described by the Holtsmark distribution [47]. Since in the laser electric field measurements the Debye length is not resolved and the measurements are further an average over

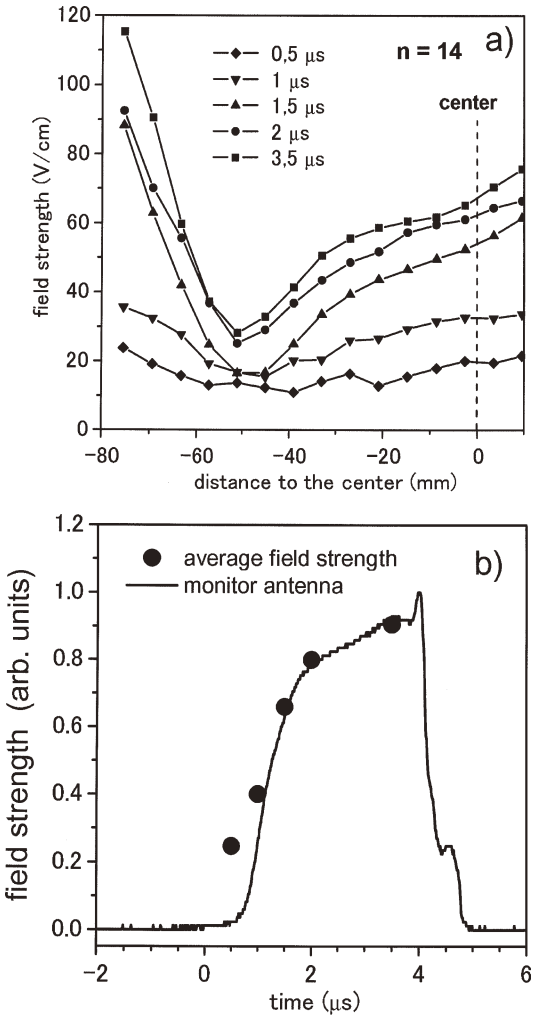

Fig. 11 Spatial distribution of the microwave field at various times after switching on the magnetron source. b) Temporal development of the spatially averaged field (dots) compared to the (uncalibrated) field measured by a monitor antenna within the ring resonator.

many successive laser shots, not the distribution itself but its average value is measured. This leads to the relation:

$$n_i = 4.86 \times 10^{14} \left(\frac{\Delta\nu}{n(n-1)} \right)^{3/2} \qquad (7)$$

Here the plasma ion density n_i is measured in cm^{-3} and the linewidth (FWHM) in cm^{-1}. n is the principal quantum number for the state of the hydrogen atom used for electric field measurement.

Density profiles at two different pressures in the above microwave discharge but with a mixture of 90% Argon and 10% Hydrogen are presented in **Fig. 12**. The solid lines show the result of a model calculation taking into account radial diffusion and recombination. Axial diffusion is neglected because of the much larger discharge length ($R^2/L^2 = 2.6 \times 10^{-2}$) and the ionization rate is much smaller than the recombination rate due to a low electron temperature of only 1.3 eV by about a factor 10^{-2}. The electron temperature was measured by a double probe using the parameterization of the Larfomboise solution provided by Peterson and Talbot [48, 49]. An analytical result can be found by an exponential function with an infinite power series in the exponent. Truncation after the first two terms yields already a satisfying agreement with the numerical solution:

$$n(\rho) \simeq n_0 \exp\left(\frac{1}{4}\rho^2 + \frac{1}{1152}\rho^6 \right) \qquad (8)$$

with

$$\rho = \frac{r}{r_0} \qquad (9)$$

and

$$r_0 = \sqrt{\frac{D_a}{k_r n_0}} \; . \qquad (10)$$

Here D_a is the ambipolar diffusion constant, k_r the recombination constant, n_0 the density in the radial centre, and r the radial position. Very good agreement of the characteristic radius r_0 obtained from a fit to the data with ab inito calculations is found by taking the measured density in the centre, the electron temperature from the probe, and the recombination rate given by Larsson ($k_r = 3.0 \times 10^{-8}$ cm^3/s) for electron H_3^+ recombination [50]. The good fit supports the model assumption that the main plasma production occurs at the edge close to the antenna where the evanescent microwave field leads to a high electron temperature. Further inwards the electron temperature decays quickly due to collisions and recombination is dominant. This results in the convex radial density profiles.

Measurements in pulsed mode a few micro seconds before and after turning off the power of the magnetron prove that the technique is independent of the electron temperature. Here, the rapid decay of the electron temperature is observed qualitatively by the vanishing plasma emission. Further, at

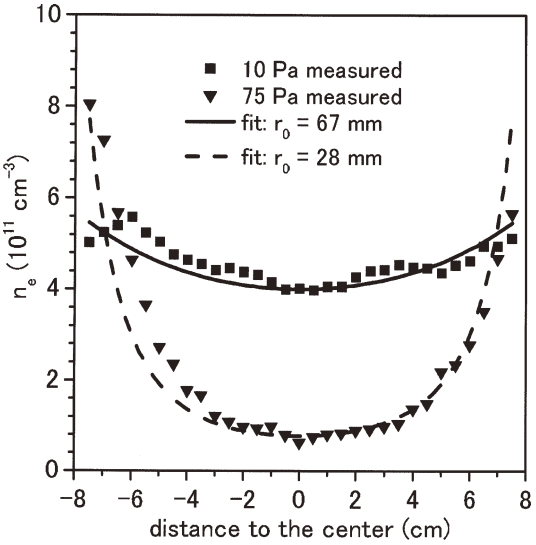

Fig. 12 Plasma density measurement in the plasma of a microwave discharge by laser electric micro field measurement. 10 Pa: squares, 75 Pa: triangles. The solid curves are fit of a radial diffusion-recombination model.

much later times (several ms), clear radial Bessel profiles are measured with a minimum resolved density of about 0.5×10^{10} cm^{-3}. The lack of any plasma background emission and the related noise in the spectra makes the afterglow measurements especially sensitive.

5. Electric Field Measurements in Argon Plasmas

As has been described in the previous section, laser-induced fluorescence-dip spectroscopy has been developed successfully using atomic hydrogen as the probe particle. The use of atomic hydrogen has an advantage in the simple Stark effects of the Rydberg states. However, the admixture of atomic hydrogen disturbs many reactive plasmas for material processing since it has chemical reactivity. The use of a rare gas is more compatible with processing plasmas. This chapter describes laser-induced fluorescence-dip spectroscopy using argon as the probe particle.

In the case of argon, the excitation from the ground state is impossible by using commercial tunable lasers even though the two-photon excitation is adopted. To realize two-step excitation shown in **Fig. 2** in argon, a metastable state $4s[3/2]^o_2$ is chosen as level 1. This metastable state is highly populated in argon-containing reactive plasmas, and is sensitively detected by laser-induced fluorescence spectroscopy. The intermediate state level 2 is chosen to be $4p[3/2]_2$, and level 3 is $4s[3/2]^o_1$. Although other excitation schemes are possible in argon, it has been shown that the above choice of the energy levels results in the simplest dip spectra of Rydberg states in the presence of electric field. The wavelengths for the excitation from $4s[3/2]^o_2$ to $4p[3/2]_2$ and for the fluorescence from $4p[3/2]_2$ to $4s[3/2]^o_1$ are 763.51 and 800.62 nm, respectively. The wavelength for the second-step excitation from $4p[3/2]_2$ to Rydberg states (level 4) is around 480 nm. The wavelengths for the first and second-step excitations are obtained by the fundamental oscillations of two tunable lasers, which is an advantage of the excitation scheme originating from the metastable $4s[3/2]^o_2$ state.

Figure 13 shows a dip spectrum observed in an inductively coupled plasma with no electric field. According to the selection rule for the electric-dipole transition in the *jl* coupling scheme, the excitation to $ns[3/2]^o_{1,2}$, $nd[1/2]^o_1$, $nd[3/2]^o_{1,2}$, and $nd[5/2]^o_{2,3}$ are possible from the intermediate $4p[3/2]_2$ state. The assignments of the dip peaks are indicated in the expanded spectrum shown in **Fig. 13(b)**. Because of the broad linewidths of the tunable lasers (0.2 and 0.25 cm^{-1} for the first and second-step excitations, respectively), several peaks are overlapped in the spectrum. The highest energy level detected by this method had a large principal quantum number of 58. Although the reduction of the laser-induced fluorescence was also observed at the shorter wavelength range, the linewidths of the tunable lasers were too broad to resolve the energy levels.

The most serious problem in using argon as the probe particle is the difficulty in calculating the complex Stark effect. To skip the complicated calculation, the Stark effect

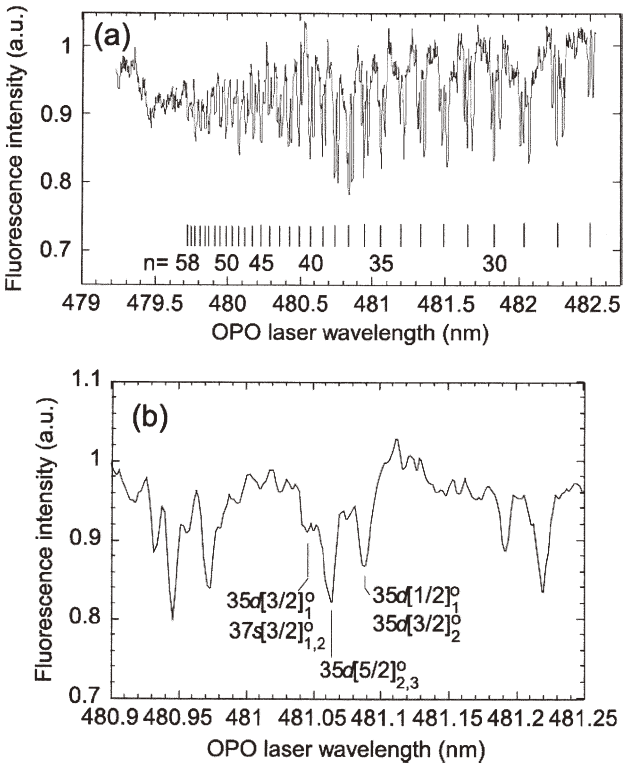

Fig. 13 (a) Example of dip spectrum obtained by exciting the intermediate $4p[3/2]_2$ state of argon to Rydberg states. The numbers n shown at the bottom of the figure indicates the principal quantum numbers of the Rydberg states. (b) Expanded spectrum of (a), showing the assignments of the dip peaks.

of argon Rydberg states was examined experimentally by transporting argon atoms at the $4s[3/2]^o_2$ state from a remote plasma source to a plasma-free region sandwiched by a pair of planar electrodes. The dip spectra were examined in well-defined electric fields, which were determined by the voltage and the distance between the electrodes. An example of the Stark spectrum of high Rydberg states with principal quantum numbers of $n = 38 - 40$ is shown in **Fig. 14**. The dip peaks observed with no electric field was assigned as shown in **Fig. 14(a)**, which is similar to the assignment shown in **Fig. 13(b)**. At a weak electric field of 6 V/cm, an additional dip peak indicated by D was observed. This dip was assigned to be the overlap of $40p[3/2]_{1,2}$ states. The transitions from the $4p[3/2]_2$ to $40p$ states are forbidden. However, in the presence of the electric field, the Stark mixing between the $40p$ and $39d[1/2]^o_1$ and $39d[3/2]^o_2$ states makes the forbidden transition observable. The energy of the $40p$ state shifted toward the low energy side with the electric field strength. Although many dip peaks may appear due to the Stark splitting at electric fields stronger than 14 V/cm, they are not resolved because of the broad linewidths of the tunable lasers. For lower Rydberg states with principal quantum numbers of 21 – 25, the Stark splitting similar to **Fig. 5** (right figure) was clearly observed [51].

Figure 15 shows a similar plot to **Fig. 5** (left figure), which shows the magnitudes of the energy shifts of the *np*

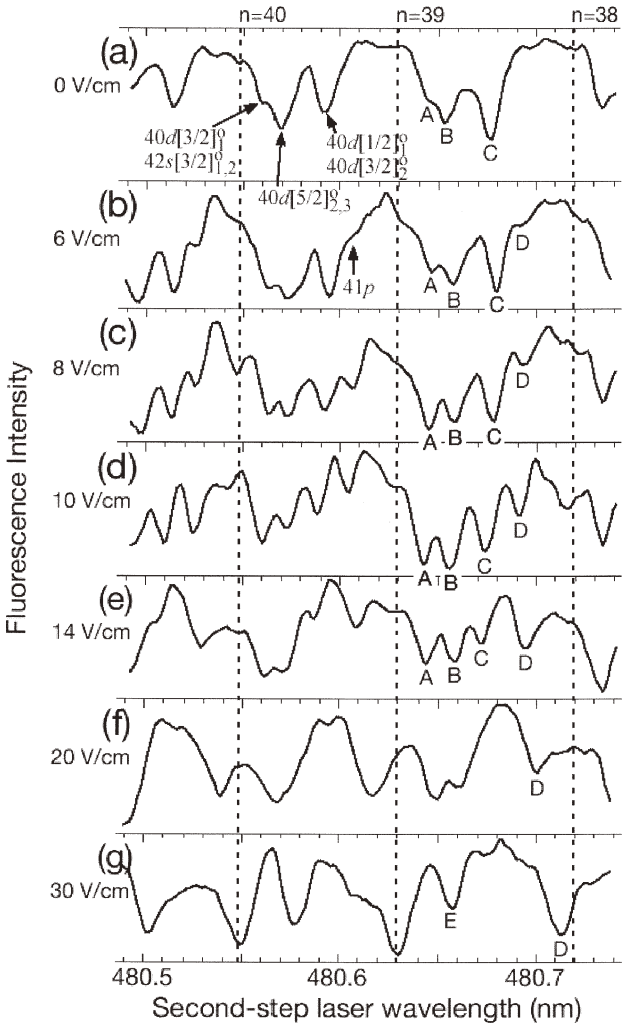

Fig. 14 Stark spectra of argon Rydberg states with principal quantum numbers of n = 38 – 40 [29].

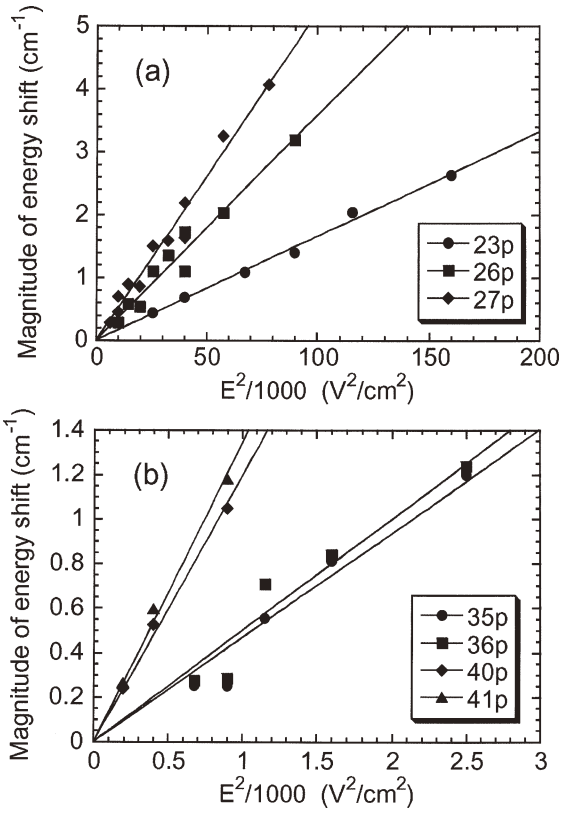

Fig. 15 Magnitudes of the energy shifts of *np* states as a function of the square of the electric field strength [51].

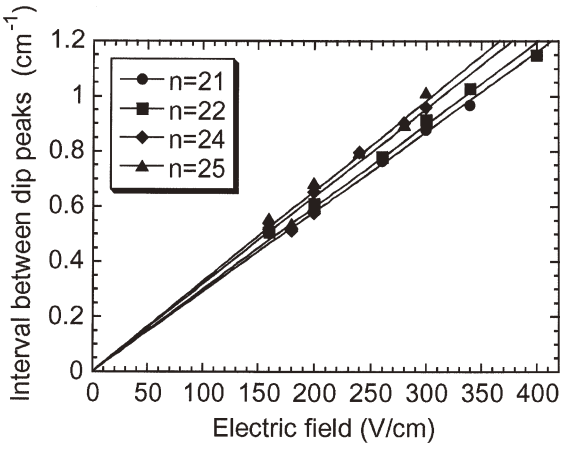

Fig. 16 Relationship between the electric field strength and the interval between the dip peaks induced by Stark splitting [51].

states as a function of the square of the electric field strength. The magnitude of the energy shift clearly indicates the quadratic Stark shift of the *np* states. On the other hand, **Fig. 16** shows the interval of the dip peaks induced by Stark splitting, indicating the linear Stark effect which is similar to **Fig. 5** (right figure). By referring to **Figs. 15** and **16**, we can determine the electric field strengths from the dip spectra obtained in argon-containing plasmas.

Figure 17 shows the distribution of the electric field strength in front of a planar electrode placed in an inductively-coupled plasma with an electron density of 3×10^{10} cm^{-3} and an electron temperature of 4 eV [30]. The discharge gas was pure argon with a pressure of 5 mTorr. The electrode was biased at −50 V with respect to the ground (chamber wall) potential. The axes of **Fig. 17** are shown by real values and normalized ones using the electron temperature and the Debye length. The horizontal error bars indicate the spatial resolution of the measurement, which is mainly determined by the ambiguity in the position of the movable electrode. The vertical error bars are evaluated from the linewidth of the tunable lasers and the ambiguity in the position of the dip peaks. The solid and dashed curves shown in **Fig. 17** represent the distribution of electric field and potential calculated by a fluid model [52], respectively. The vertical dotted line indicates the position of the sheath edge according to the conventional definition (the velocity of ion fluid has the Bohm velocity at the sheath edge). As seen from **Fig. 17**, the distribution of the experimental electric field in the sheath region was consistent with the theoretical result. On the other hand, the strength of the electric field in the presheath region was higher than the theoretical electric field. This discrepancy may be explained

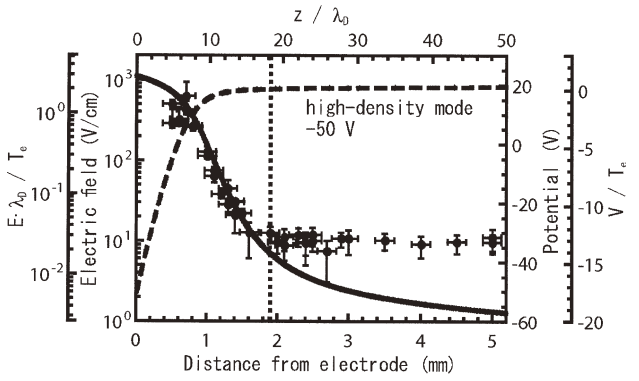

Fig. 17 Distribution of electric field in front of a planer electrode placed in an inductively-coupled argon plasma [30]. The solid and dashed curves represent the electric field and the potential calculated by a fluid model.

by the presence of microfield. The electric field strengths in the presheath region were evaluated from the Stark spectra of the energy level with $n = 41$, which is so sensitive that the Stark spectrum is affected by the microfield.

The measurement of the sheath electric field was repeated in an electronegative plasma by adding SF_6 into argon [31]. **Figure 18(a)** shows the distribution of the electric field observed at an SF_6 percentage of 10%. The total gas pressure was 10 mTorr, and the electrode was biased at −20 V with respect to the ground potential. The electron density and the ratio of the negative ion density to the electron density (n_-/n_e) were 4×10^8 cm^{-3} and 29, respectively. In the case of the electronegative plasma, it was observed that the sheath electric field had a stepwise structure. The constant electric field at $z >$ 2.6 mm may be due to the microfield. The stepwise change in the electric field strength at $z = 2.6$ mm is due to the localized reflection of negative ions by the weak electric field, resulting in the high space charge density shown in **Fig. 18(b)**, which was obtained by calculating the divergence of the theoretical electric field shown in **Fig. 18(a)**. This localized reflection is caused by the fact that the negative ion temperature is much lower than the electron temperature. This is the first direct observation of the stepwise structure of the sheath electric field in an electronegative plasma.

6. Summary and Outlook

The measurement of electric field by laser-induced fluorescence-dip spectroscopy is much more sensitive than conventional Stark spectroscopy. In addition, it has advantages in the high spatial and temporal resolutions and the applicability to plasmas with various discharge geometries and discharge conditions. Owing to the excellent features of laser-induced fluorescence-dip spectroscopy, it has become possible to investigate the structure of sheath electric field in plasmas used for material processing. Investigations on electric fields in sheaths and plasmas are significantly insufficient even though they play an essential role in material processing as well as discharge physics. The development of laser-induced fluorescence-dip spectroscopy opens a new area in the research field of low-temperature plasma diagnostics.

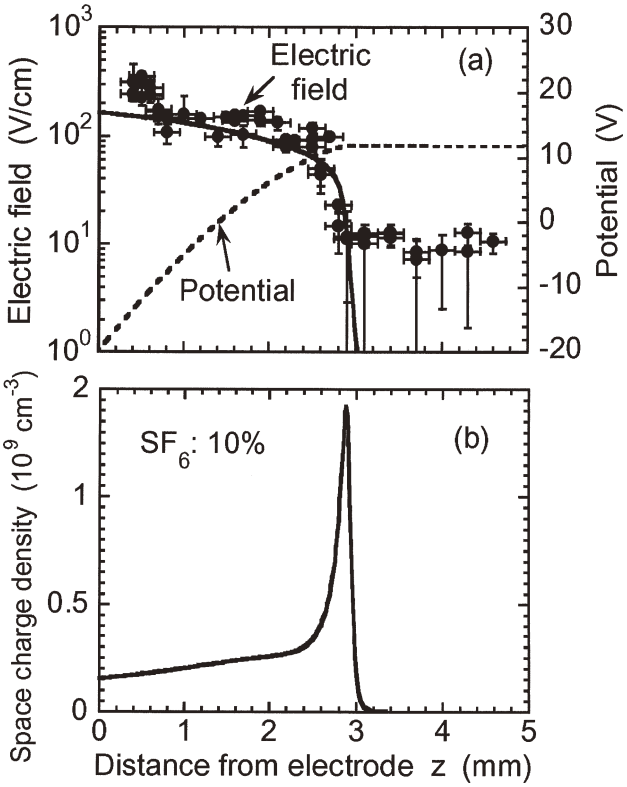

Fig. 18 (a) Distribution of electric field in front of a planer electrode placed in an inductively-coupled Ar/SF_6 plasma [31]. (b) Space charge density calculated from the theoretical electric field shown by the solid curve in (a).

Acknowledgments

The work on electric field measurements in hydrogen and krypton was supported by grants from the Bundesministerium für Forschung und Technologie (BMBF), the Ministerium für Innovation, Wissenschaft, Forschung und Technologie NRW (MIWFT), and the Deutsche Forschungsgemeinschaft (DFG) in the frame of SFB 591. Further, the invaluable contribution of Dr. Luggenhölscher is gratefully acknowledged. The work on electric field measurements in argon was supported by JSPS KAKENHI (16340181 and 13480124), and was also supported partly by 21st century COE (Center of Excellence) program "Information Nano-Devices Based on Advanced Plasma Science" of Nagoya University. The results on argon was obtained by the excellent contribution of Dr. Takizawa. One of the authors (UCZ) wants to thank Prof. Hideo Sugai and Prof. Toshiaki Makabe for providing ideal working conditions for preparing this manuscript during a sabbatical stay in Japan.

References

[1] F.F. Chen in M.N. Hirsch and H.J. Oskam (edit.), *Gaseous Electronics, Vol. 1* (Academic Press, New York 1978).

[2] T. Lho, N. Hershkowitz and G.H. Kim, Rev. Sci. Instrum. **71**, 403 (2000).

[3] R. Piejak, V. Godyak and B. Alexandrovich, Rev. Sci. Instrum. **72**, 4002 (2001).
[4] H.R. Griem, *Spectral Line Broadening by Plasmas* (Academic Press, New York 1974).
[5] J.E. Lawler and D.A. Doughty, Adv. At. Mol. Opt. Phys. **34**, 171 (1994).
[6] K. Muraoka, M.D. Bowden, J.B. Kim, K. Kawamura and K. Uchino, J. Plasma Fusion Res. **75**, 275 (1999) [*in Japanese*].
[7] R.A. Gottscho, Phys. Rev. A **36**, 2233 (1987).
[8] B.N. Ganguly, J. Appl. Phys. **60**, 571 (1986).
[9] E.A. Den Hartog, D.A. Doughty and J.E. Lawler, Phys. Rev. A **38**, 2471 (1988).
[10] M.P. Alberta, H. Debontride, J. Derouard and N. Sadeghi, J. Phys. III (France), **3**, 105 (1993).
[11] K.E. Greenberg and G.A. Hebner, Appl. Phys. Lett. **63**, 3282 (1993).
[12] G.A. Hebner, K. Greenberg and M.E. Riley, J. Appl. Phys. **76**, 4036 (1994).
[13] J.P. Booth, M. Fadlallah, J. Derouard and N. Sadeghi, Appl. Phys. Lett. **65**, 819 (1994).
[14] J.P. Booth, M. Fadlallah, J. Derouard and N. Sadeghi, Appl. Phys. Lett. **69**, 1361 (1994).
[15] Y.W. Choi, M.D. Bowden and K. Muraoka, Appl. Phys. Lett. **69**, 1361 (1996).
[16] S. Maurmann, V.P. Gavrilenko, H.J. Kunze and E. Oks, J. Phys. D: Appl. Phys. **29**, 1525 (1996).
[17] U. Czarnetzki, D. Luggenhölscher and H.F. Döbele, Phys. Rev. Lett. **81**, 4592 (1998).
[18] J.B. Kim, K. Kawamura, Y.W. Choi, M.D. Bowden, K. Muraoka and V. Helbig, IEEE Trans. Plasma Sci. **26**, 1556 (1998).
[19] U. Czarnetzki, D. Luggenhölscher and H.F. Döbele, Plasma Sources Sci. Technol. **8**, 230 (1999).
[20] U. Czarnetzki, D. Luggenhölscher and H.F. Döbele, Appl. Phys. A **72**, 509 (2001).
[21] U. Czarnetzki, G.A. Hebner, D. Luggenhölscher, H.F. Döbele and M.E. Riley, IEEE Trans. Plasma Sci. **27**, 70 (1999).
[22] U. Czarnetzki, D. Luggenhölscher, V.A. Kadetov and H.F. Döbele, Pure Appl. Cem. **77**, 345 (2005).
[23] J.B. Kim, T. Ikutake, M.D. Bowden, K. Muraoka and U. Czarnetzki, Jpn. J. Appl. Phys. **39**, 299 (2000).
[24] V.P. Gavrilenko, H.J. Kim, T. Ikutake, J.B. Kim, Y.Y.W. Choi, M.D. Bowden and K. Muraoka, Phys. Rev. E **62**, 7201 (2000).
[25] V.P. Gavrilenko, Instr. Exp. Tech. **49**, 149 (2006).
[26] E.K. Cherkasova, V.P. Gavrilenko and A.I. Zhuzhunashvili, J. Phys. D: Appl. Phys. **39**, 477 (2006).
[27] Z. Altug, J. Neumann, T. Rieper and V. Helbig, *Proc. 10th International Symposium on Laser-Aided Plasma Diagnostics*, edited by K. Muraoka (Fukuoka, Japan, 2001).
[28] E. Wagenaars, G.M.W. Kroesen and M.D. Bowden, Phys. Rev. A **74**, 033409 (2006).
[29] K. Takizawa, K. Sasaki and K. Kadota, Jpn. J. Appl. Phys. **41**, L1285 (2002).
[30] K. Takizawa, K. Sasaki and A. Kono, Appl. Phys. Lett. **84**, 185 (2004).
[31] K. Takizawa, A. Kono and K. Sasaki, Appl. Phys. Lett. **90**, 011503 (2007).
[32] T. Jiang, M.D. Bowden, E. Wagenaars, E. Stoffels and G.M.W. Kroesen, New J. Phys. **8**, 202 (2006).
[33] E.V. Barnat and G.A. Hebner, Appl. Phys. Lett. **85**, 3393 (2004).
[34] T. Kampschulte, J. Schulze, D. Luggenhölscher, M.D. Bowden and U. Czarnetzki, New J. Phys. **9**, 18 (2007).
[35] M. Watanabe, K. Takiyama and T. Oda, Rev. Sci. Instrum. **70**, 903 (1999).
[36] M. Watanabe, K. Takiyama and T. Oda, Jpn. J. Appl. Phys. **39**, L116 (2000).
[37] O.A. Evsin, E.B. Kupryanova, V.A. Ochkin, S. Yu. Savinov and S.N. Tskhai, Quant. Electr. **25**, 278 (1995).
[38] V.N. Ochkin, S.Y. Savinov, S.N. Tskhai, U. Czarnetzki, V. Schulz-von der Gathen and H.F. Döbele, IEEE Trans. Plasma Sci. **26**, 1502 (1998).
[39] M.I. de la Rosa, C. Perez, K. Grutzmacher, A.B. Gonzalo and A. Steiger, Plasma Sources Sci. Technol. **15**, 105 (2006).
[40] N. Sadeghi, D.W. Setser, A. Francis, U. Czarnetzki and H.F. Döbele, J. Chem. Phys. **115**, 3144 (2001).
[41] R.D. Cowan, *The theory of atomic structure and spectra* (University of California Press, London 1981).
[42] H.A. Bethe and E.E. Salpeter, *Quantum Mechanics of One- and Two-Electron Atoms* (Springer Verlag, Berlin, 1957).
[43] T. Ebata, N. Mikami and M. Ito, J. Chem. Phys. **78**, 1132 (1983).
[44] U. Czarnetzki, T. Mussenbrock and R.P. Brinkmann, Phys. Plasmas **13**, 123503 (2006).
[45] D. Luggenhölscher, U. Czarnetzki and H.F. Döbele, *Proceedings of International Symposium on Laser Aided Plasma Diagnostics* (Snowbird, Utah, USA, September 26-29, 2005).
[46] F. Werner, D. Korzec and J. Engemann, Plasma Sources Sci. Technol. **3**, 473 (1994).
[47] J. Holtsmark, Ann. Phys. **58**, 577 (1919).
[48] J. Lafamboise, University of Toronto, Institute for Aerospace Studies, Report No. 100 (1966).
[49] E. Peterson, L. Talbot, Aeronautical Sciences Division Rept. AS-69-12, Univ. of California, Berkeley (1969).
[50] M. Larsson, Phil. Trans. Royal Soc. Lond. A **358**, 2433 (2000).
[51] K. Takizawa and K. Sasaki, *submitted to* Phys. Rev. A.
[52] A. Kono, J. Phys. D **32**, 1357 (1999).